Nanoscale

ROYAL SOCIETY OF CHEMISTRY

PAPER

View Article Online
View Journal | View Issue

Cite this: *Nanoscale*, 2023, **15**, 17922

Carbonized polymer dots derived from metformin and L-arginine for tumor cell membrane- and mitochondria-dual targeting therapy†

Manling Chen,[a] Yang Li,[b] Yangcheng Liu,[c] Baohua Jia,[d] Xue Liu *[a] and Tianyi Ma *[d]

Metformin has demonstrated antitumor potential in clinical studies; however, achieving optimal antitumor effects requires administering an extremely safe medication dose. To enhance the efficacy and reduce dosage requirements, we propose the creation of large-molecule drugs through the combination of small-molecule drugs. In this study, we developed novel polymer dots, referred to as MA-dots, with sizes of approximately 5 nm, featuring dual targeting capabilities for tumor cell membranes and mitochondria. MA-dots were synthesized using metformin and L-arginine *via* a rapid microwave-assisted method. Notably, the resulting MA-dots (with a half maximal inhibitory concentration (IC_{50}) of 93.60 μg mL^{-1}) exhibited more than a 12-fold increase in antitumor activity compared to the raw metformin material (IC_{50} = 1159.00 μg mL^{-1}) over a 24-hour period. In addition, our MA-dots outperformed most metformin-derived nanodrugs in terms of antitumor efficacy. Furthermore, oral gavage treatment with MA-dots led to the suppression of A549 (lung cancer cell lines) tumor growth *in vivo*. Mechanistic investigations revealed that MA-dots bound to the large neutral amino acid transporter 1 (LAT1) proteins, which are overexpressed in malignant tumor cell membranes. Moreover, these MA-dots accumulated within the mitochondria, leading to increased production of reactive oxygen species (ROS), mitochondrial damage, and disruption of energy metabolism by modulating the 5′-adenosine monophosphate-activated protein kinase (AMPK)/mammalian target of rapamycin (mTOR) pathway in tumor cells. This cascade of events triggers cell-cycle arrest and apoptosis. In summary, this study presented a rapid method for fabricating a novel nanoderivative, MA-dots, capable of both tumor targeting and exerting tumor-suppressive effects.

Received 17th August 2023,
Accepted 12th October 2023

DOI: 10.1039/d3nr04145j

rsc.li/nanoscale

1. Introduction

Metformin, a commonly employed oral antidiabetic medication, is reported to exhibit a certain degree of tumor cell proliferation suppression and apoptosis induction.[1] Its antitumor effect manifests through the induction of cell cycle arrest and the activation of the apoptotic pathways.[2,3] The long-term clinical use of metformin has numerous advantages, including minimal adverse effects, low clinical risk, and excellent tolerability. Particularly noteworthy is its application in type-2 diabetes patients with malignancies, where metformin therapy enables the maintenance of reasonable glycemic control and provides additional clinical benefits in tumor treatment.[4–6] However, when administered at repeatedly high doses, metformin exhibits limited additional antitumor activity in patients with tumors.[7] This limitation primarily stems from the restricted cellular uptake of metformin.[8] The high doses required for its antitumor function far exceed the standard antidiabetic doses,[9,10] potentially resulting in severe side effects such as gastrointestinal symptoms and relatively rare occurrences of lactic acidosis.[11] Therefore, future clinical use of metformin in tumor therapy necessitates selective enhancement of tumor cell uptake efficiency and a reduction in the medication threshold.

Carbonized polymer dots (CPDs) are zero-dimensional carbon nanomaterials that have garnered substantial attention in biomedicine owing to their exceptional properties.[12,13] CPDs can be administered conveniently through either injec-

[a]*Institute of Clean Energy Chemistry, Key Laboratory for Green Synthesis and Preparative Chemistry of Advanced Materials, College of Chemistry, Liaoning University, Shenyang 110036, Liaoning, P. R. China. E-mail: liuxue@lnu.edu.cn*
[b]*Department of Cell Biology, Key Laboratory of Cell Biology of Ministry of Public Health, Key Laboratory of Medical Cell Biology of Ministry of Education, China Medical University, Shenyang 110122, Liaoning, P. R. China*
[c]*School of Pharmaceutical Science, Liaoning University, Shenyang 110036, Liaoning, P. R. China*
[d]*School of Science, STEM College, RMIT University, Melbourne, VIC 3000, Australia. E-mail: tianyi.ma@rmit.edu.au*

† Electronic supplementary information (ESI) available. See DOI: https://doi.org/10.1039/d3nr04145j

tion or oral intake, ensuring effective integration into the *in vivo* environment.[14–16] Their favorable solubility and biomacromolecule-like size significantly facilitate the penetration of various biological barriers.[17] They can be readily functionalized to enhance tumor-targeting capabilities and serve as drug-delivery vehicles.[18–20] Their outstanding biocompatibility and minimal toxicity revealed in both *in vitro* and *in vivo* studies further underscore their promise in biomedicine.[15,21,22] Recent investigations have revealed that CPDs derived from conventional small-molecule drugs can augment their original pharmacological properties and mitigate their toxic side effects in normal cells. In fact, these CPDs often exhibit superior therapeutic effects compared with the original drugs. For instance, berberine CPDs demonstrated exceptional water solubility and tumor accumulation, resulting in enhanced *in vivo* antitumor activity compared with free berberine (approximately a two-fold increase).[23] Aspirin CPDs exhibited efficient cellular internalization, enhanced inhibitory effects on TNF-α and IL-1β, and an ability to regulate inflammatory responses.[24] Highly soluble levofloxacin CPDs demonstrated antimicrobial activity more than 500 times higher than insoluble levofloxacin.[25] Furthermore, the CPDs derived from curcumin exhibited a 1000-fold higher antiviral capacity and 34-fold greater biocompatibility than curcumin itself.[26] Han *et al.* synthesized CPDs through the hydrothermal treatment of adenosine and aspirin,[27] resulting in CPDs with superior cytocompatibility and biosafety compared to their precursors (more than a two-fold increase), which directed the osteogenic differentiation of the human bone marrow mesenchymal stem cells.

Based on these results, it is worthwhile to explore a novel design and fabrication strategy for transforming metformin into metformin CPDs, potentially overcoming the limitations encountered in the current use of metformin in tumor treatment. A recent study by Wan *et al.* involved mixing metformin with citric acid to prepare CPDs aimed at suppressing tumor cell growth. However, these CPDs did not exhibit significant cytotoxicity against A549 (lung cancer cell lines) cells until the concentration reached 1000 μg mL^{-1} under the normal-glucose conditions for 72 h.[28]

In the present study, a novel well-soluble antitumor nanoderivative, hereafter referred to as MA-dots, was synthesized through a straightforward microwave treatment involving metformin and L-arginine (Scheme 1). The MA-dots exhibited the characteristic morphology of classical CPDs, presenting as small-size globular carbon nanoparticles measuring approximately 5 nm in size. The formation mechanism and potential structure of MA-dots were elucidated. Specifically, metformin contributed to the formation of the triazine framework within the MA-dot precursor, whereas L-arginine played a pivotal role as a passivation agent, stabilizing this framework. Consequently, the MA-dots retained their antitumor activity

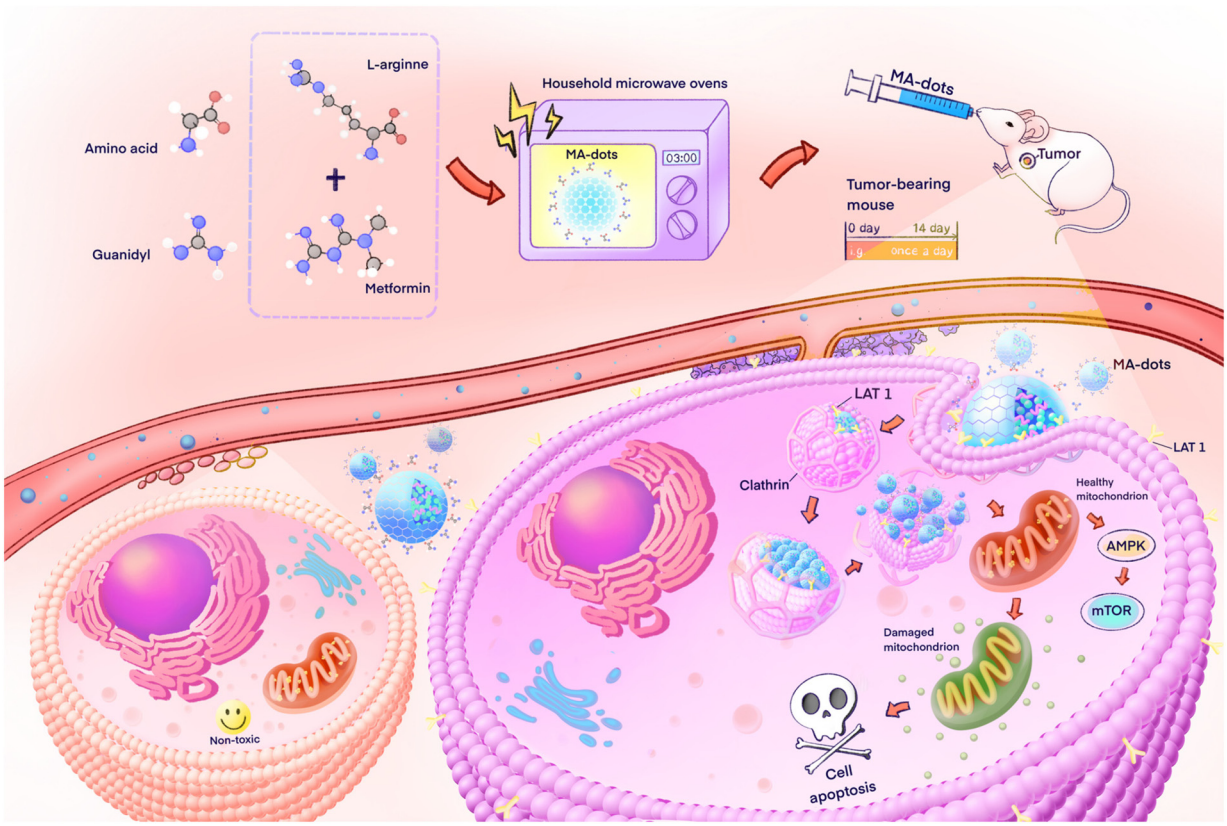

Scheme 1 Diagram depicting the fabrication of the MA-dots for tumor-targeted treatment.

and specifically targeted both tumor cell membranes and mitochondria. These MA-dots were capable of binding to the large neutral amino acid transporter 1 (LAT1) proteins, which are known for their high expression in malignant tumor cell membranes. This tumor-specific targeting mechanism facilitated substantial accumulation of the MA-dots within tumor cells and tissues, as evidenced by their autofluorescence. Once inside the tumor cells, MA-dots like metformin accumulated within the mitochondria, a phenomenon verified through colocalization studies. Subsequently, MA-dots inhibited tumor development by inducing increased production of reactive oxygen species (ROS), causing damage to the mitochondrial structure, disrupting energy metabolism, and ultimately leading to cell cycle arrest and apoptosis. Notably, the half maximal inhibitory concentration (IC_{50}) of the tumor cells treated with MA-dots (IC_{50} = 93.60 μg mL^{-1}) decreased by more than 12-fold compared to those treated with metformin (IC_{50} = 1159.00 μg mL^{-1}) over a 24-hour period. Furthermore, oral administration of MA-dots in an A549 tumor-bearing mouse model confirmed their *in vivo* antitumor activity.

2. Materials and methods

2.1. Materials

Metformin hydrochloride (Met, >98%), L-arginine (Arg, 99%), L-phenylalanine (Phe, 99%), L-leucine (Leu, >99%), glycine (Gly, 99%), and dimethyl sulfoxide were obtained from Shanghai Adamas Reagent Co. Ltd (Shanghai, China). 2-Amino bicyclo-(2,2,1)-heptane-2-carboxylic acid (BCH, 95%) was obtained from Macklin Biochemical Co. Ltd (Shanghai, China). Chlorpromazine and genistin were purchased from Sigma-Aldrich Co. Ltd (Munich, Germany). Bovine serum albumin (BSA) was acquired from Solarbio Life Science Co. Ltd (Beijing, China). Hoechst 33342, Mito-tracker, methyl thiazolyl diphenyl-tetrazolium bromide (MTT), mitochondrial membrane potential (MMP) assay kit, 2',7'-dichlorodihydrofluorescein diacetate (DCFH-DA), annexin V-FITC/propidium iodide (PI) apoptosis assay kit, cell cycle and apoptosis assay kit, and bicinchoninic acid (BCA) protein assay kit, cyclin A2 rabbit polyclonal antibody (AF6624, diluted 1 : 1000 with 3% BSA), and cyclin B1 rabbit polyclonal antibody (AF6627, diluted 1 : 1000 with 3% BSA) were obtained from Beyotime Biotechnology Co. Ltd (Shanghai, China). Enhanced radioimmunoprecipitation precipitation assay (RIPA) lysis buffer, phosphatase inhibitor cocktail, phenylmethanesulfonyl fluoride (PMSF), and paraformaldehyde were ordered from Servicebio Biotechnology Co. Ltd (Wuhan, China). Primary antibodies against 5'-adenosine monophosphate-activated protein kinase α (AMPKα) (ab32047, diluted 1 : 1000 with 3% BSA), phosphorylated AMPKα (p-AMPKα) (ab92701, diluted 1 : 1000 with 1% BSA), mammalian target of rapamycin (mTOR) (ab134903, diluted 1 : 1000 with 3% BSA), and phosphorylated mTOR (p-mTOR) (ab109268, diluted 1 : 1000 with 3% BSA) were purchased from Abcam Co. Ltd (Cambridge, UK). β-Actin antibody (AF7018, diluted 1 : 5000 with 3% BSA) and the secondary antibody (S0001, diluted 1 : 5000 with 3% BSA), horseradish peroxidase (HRP)-conjugated goat anti-rabbit IgG (H + L), were from Affinity Biosciences Co. Ltd (Changzhou, China). All cell growth plates were purchased from NEST Biotechnology Co. Ltd (Wuxi, China). Ultrapure water (18.2 Ω) from a Milli-Q system (Merck, Germany) was used throughout the experiments.

2.2. Characterization of MA-dots

Fourier-transform infrared (FT-IR) spectra were obtained from an FT-IR spectrometer (PerkinElmer, Waltham, US). KBr pellets were used to disperse the powder samples. X-ray photoelectron spectroscopy (XPS) spectra were obtained from a K-Alpha XPS system (Thermo Scientific, Massachusetts, US). Transmission electron microscopy (TEM) studies were carried out using the JEM-2100 high-resolution electron microscope (JEOL, Tokyo, Japan) or Hitachi HT7700 electron microscope (Hitachi, Tokyo, Japan). Powder X-ray diffraction (XRD) measurements were conducted on a D8 Advance X-ray diffractometer (Bruker, Karlsruhe, Germany). The ultraviolet–visible (UV-vis) absorption spectra were obtained from a TU-1900 UV-vis absorption spectrophotometer (Purkinje General, Beijing, China). Fluorescence spectra were obtained from an RF-5301PC fluorescence spectrophotometer (Shimadzu, Kyoto, Japan). Flow cytometry experiments were conducted on an Accuri C6 plus flow cytometer (Accuri Cytometers, Ann Arbor, US) or a FACSCalibur flow cytometer (BD Biosciences, San Jose, US). Cell imaging was carried out using a Ts2 inverted microscope (Nikon, Tokyo, Japan).

2.3. Synthesis of the MA-dots

The MA-dots were prepared *via* a microwave-mediated method as follows. First, 0.50 g Met (MW = 165.63 g mol^{-1}) and 0.53 g Arg (MW = 174.20 g mol^{-1}) were dissolved in 10 mL water. The solution was dissolved entirely after sonicating for 5 min using a KH-400KDB ultrasonic cleaner (Hechuang Ultrasonic Equipment, Kunshan, China). Subsequently, the solution was heated for 3 min using a microwave reactor (Midea Microwave, Foshan, China). A dark brown clustered solid was collected from the container. The solid was cooled to room temperature and dissolved in 10 mL water, assisted by sonication. The crude MA-dot solution was centrifuged (5000 rpm, 5 min) to eliminate undissolved precipitates using a TGL-16 centrifuge (Xiangyi, Hunan, China). The supernatant was then filtered through a 0.22 μm filter membrane (Spectrum Labs, Rancho Dominguez, US). The filtrate was dialyzed using a 500–1000 Da dialysis membrane (Spectrum Labs, Rancho Dominguez, US) for 24 h. The pure MA-dot powder was obtained by freeze-drying the dialysate using an FDU-1200 lyophilizer (EYELA, Tokyo, Japan).

2.4. Cell uptake

The A549 and BEAS-2B (normal lung epithelial cell lines) cells were cultured in 6-well plates (1×10^5 cells per well). After 24 h of incubation, the cells were incubated with the MA-dots (100 μg mL^{-1}) for another 6 h. Then, the cells were washed

three times with PBS and analyzed by inverted fluorescence microscopy and flow cytometry.

To check the feature of the large neutral amino acid analogues of the MA-dots, the A549 cells were pretreated with 5 mM amino acids (including Leu, Phe, and Gly) or inhibitors (including 5 mM BCH, 20 μM chlorpromazine, and 50 μM genistein) for 1 h before being treated with the MA-dots.

2.5. Cell viability analysis

Cell viability was assessed by the MTT method. In detail, various cells were seeded in 96-well plates (1×10^4 cells per well) with a specific culture medium for 24 h. Then, a fresh culture medium containing various concentrations (0, 25, 50, 100, 150, and 200 μg mL^{-1}) of the MA-dots or Met or Arg was added after the culture medium was removed. After 24 h of incubation, each well was washed with 100 μL MTT (5 mg mL^{-1}), and the cells were incubated for another 4 h. Subsequently, the MTT solution was carefully aspirated, followed by dissolving with 150 μL dimethyl sulfoxide per well. Absorbance was conducted at 570 nm using a FLUOstar Omega microplate reader (BMG Labtech, Offenburg, Germany).

2.6. Cell apoptosis and cycle analysis

The A549 cells were cultured in 6-well plates (1×10^5 cells per well). Then, the culture medium was changed to a 2 mL culture medium containing the MA-dots or Met (50 μg mL^{-1}). After 24 h of incubation, the cells were washed and harvested with PBS. Afterward, the cells were treated with annexin V-FITC/PI for cell apoptosis assay based on the kit instructions. The cells were treated with RNase and stained with PI for cell cycle assay.

2.7. Colocalization imaging

The A549 cells were cultured in 12-well plates (3×10^4 cells per well) for 24 h. A fresh culture medium containing the MA-dots was then added after the culture medium was removed. After incubating for 8 h, the cells were washed with PBS and imaged using an inverted microscope. Fluorescence imaging was carried out by using Mito-tracker (50 nM) and Hoechst 33342 (5 μg mL^{-1}) to process the PBS-washed cells for 30 min before imaging. Analysis of Pearson's correlation coefficient was performed by Image J software using Coloc2 analysis.

2.8. MMP measurement

The A549 cells were cultured in 6-well plates (1×10^5 cells per well). Then, the culture medium was changed to a 2 mL culture medium containing the MA-dots or Met (100 μg mL^{-1}). After 24 h of incubation, the cells were washed and harvested with PBS. Afterward, the cells were treated with 1 μM JC-1 for MMP assay based on the kit instructions. The mitochondrial morphology was observed before staining using an HT7800 high-resolution electron microscope (Hitachi, Tokyo, Japan).

2.9. ROS measurement

The A549 cells were cultured in 6-well plates (1×10^5 cells per well). Then, the culture medium was changed to a 2 mL culture medium containing the MA-dots or Met (100 μg mL^{-1}). After 24 h of incubation, the cells were washed and harvested with PBS. Afterward, the cells were treated with 10 μM DCFH-DA at 37 °C for 30 min for ROS assay before fluorescence imaging and flow cytometry analysis.

2.10. Animals

Female BALB/c nude mice (5–6 weeks) were purchased from the Vital River Laboratory Animal Technology Co. Ltd (Beijing, China). Healthy female BALB/c mice (5–6 weeks) were supplied by Liaoning Changsheng Biotechnology CO. Ltd (Benxi, China). The animal experimental procedures were conducted following the recommendations of the Animal Ethics Committee of China Medical University (assigned approval number: no. 2023656). Under a 12 h/12 h darkness/light cycle, the mice were kept in a specific-pathogen-free (SPF) barrier environment with a 40–70% humidity at 25 °C.

2.11. Xenograft tumor model

BALB/c nude mice (about 20 g) were subcutaneously inoculated with A549 tumor cells (1×10^7 cells per mouse) in the left axilla. When tumors reached approximately 50 mm^3 (tumor volume = tumor length × tumor width × tumor width × 0.5), various drugs were administered to the mice.

2.12. *Ex vivo* fluorescence imaging of the organs and tumors

After oral administration of the MA-dots (dose: 100 mg kg^{-1}), the tumor-bearing mice were sacrificed at 2, 4, 6, 16, and 24 h. The organs, including the heart, lungs, spleen, liver, kidneys, stomach, and small intestine, were harvested and observed by immediate fluorescence imaging using an IVIS system (Caliper Lifesciences, Waltham, US). The fluorescence images were obtained at 480 nm excitation and 520 nm emission. The images were analyzed using the Living Image 4.2 software (Caliper Life Science, Hopkinton, USA) with the same settings for data consistency.

2.13. *In vivo* therapy

The tumor-bearing mice were randomly split into three groups (n = 5) and administered through everyday oral gavage with various formulations, including (1) 1 mL of water (control), (2) Met dispersed in 1 mL of water (100 mg kg^{-1}), and (3) the MA-dots dispersed in 1 mL of water (100 mg kg^{-1}). The tumor volume was monitored on the selected days (0, 3, 6, 9, and 12 d). The tumor-bearing mice were sacrificed on day 14 after the last gavage. The tumor was removed from the body and weighed. The tumors were cut into slides and visualized under light microscopy after hematoxylin–eosin (H&E), Ki67, and terminal transferase dUTP nick end labeling (TUNEL) staining.

2.14. Western blot analysis

The A549 cells and tumor tissues treated with the MA-dots or Met according to the method above were extracted in a lysis buffer solution using protease and phosphatase inhibitors, respectively. The total protein concentration was detected by the BCA method. Equal amounts of denatured proteins were isolated *via* SDS-PAGE gel and transferred to the PVDF membranes. The membranes were probed with the antibodies against cyclin A2, cyclin B1, AMPK, p-AMPK, mTOR, p-mTOR, and β-actin and then incubated with an HRP-labelled secondary antibody. The proteins were captured using an ECL detection kit (Beyotime, Shanghai, China) on a Tanon-5200 chemiluminescence image analysis system (Tanon Science & Technology, Shanghai, China). Images were analyzed using Image J software.

2.15. Statistical analysis

The data were represented as the mean ± standard deviation (s.d.). Unpaired Student's *t*-test (two-tailed) was used to compare the two groups. One- or two-way ANOVA was carried out to analyze the statistical significance among more than two groups. Statistical analysis was conducted with GraphPad Prism 10.0.2 software (GraphPad Software, San Diego, US).

3. Results and discussion

3.1. Chemical structure and formation mechanism of the MA-dots

The synthesis of MA-dots involved microwave treatment with metformin and L-arginine. The proposed mechanism for the formation of MA-dots is shown in Fig. 1a. Initially, condensation polymerization occurred between metformin molecules, and in the presence of HCl and H_2O, intermolecular guanidine groups underwent a reaction, leading to the formation of a six-membered triazine ring after deamidation. The triazine ring continued to grow with the addition of metformin. Subsequently, L-arginine, acting as a passivation agent, reacted with the active edge atoms of the multimeric ring structure. The guanidine groups from the two L-arginine molecules participated in the formation of a new six-membered triazine ring by reacting with the fringe C–N–C structure of the two triazine rings. During the microwave heating process, C=C and C=N

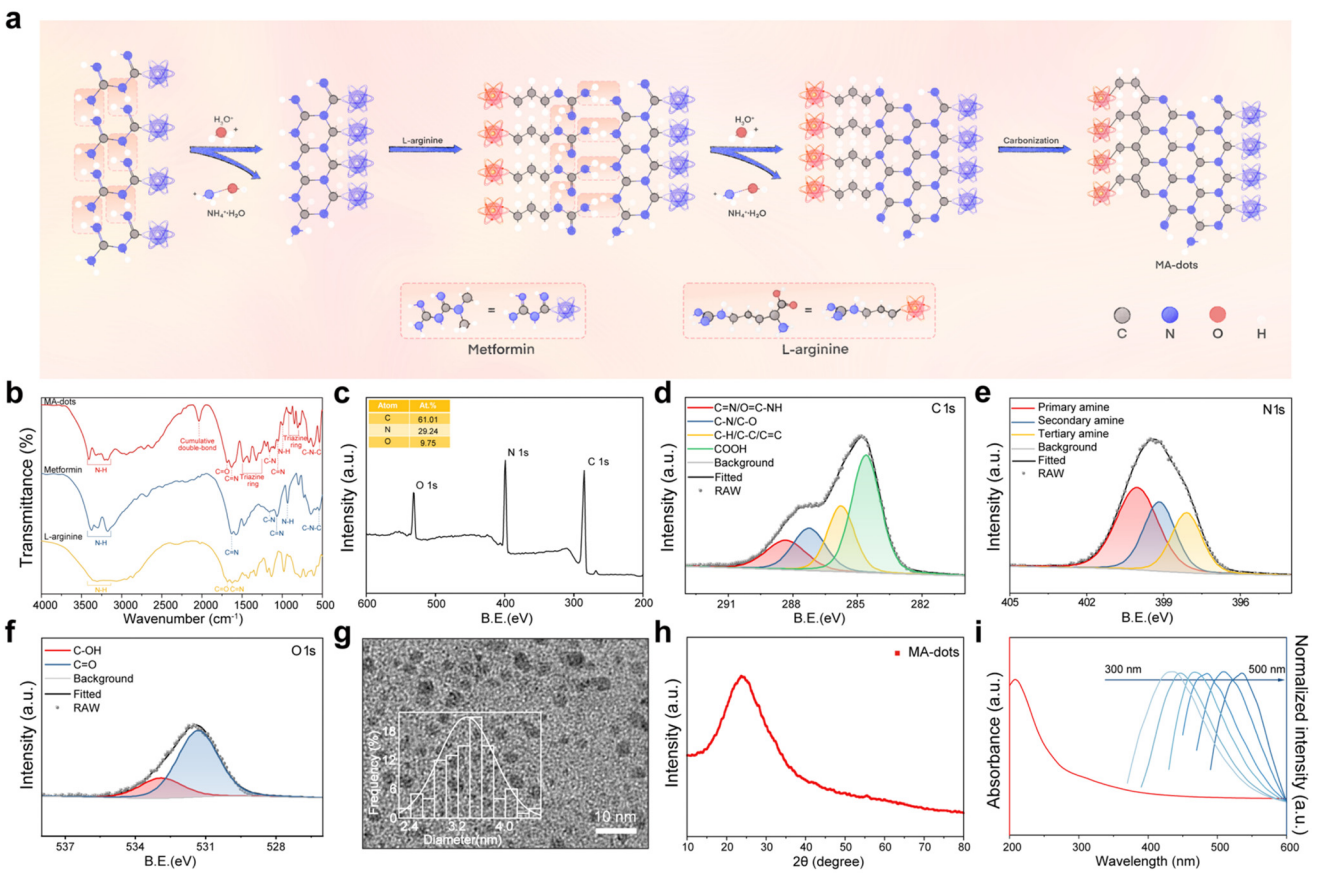

Fig. 1 Formation mechanism and chemical structure of the MA-dots. (a) Possible formation mechanism of the MA-dots. (b) FT-IR spectra of the MA-dots (red), metformin (blue), and L-arginine (yellow). (c) XPS survey spectrum of the MA-dots. The deconvoluted C 1s (d), N 1s (e), and O 1s (f) spectra of the MA-dots. (g) TEM image of the MA-dots. Scale bar = 10 nm. Inset, the size distribution of the MA-dots. (h) XRD patterns of the MA-dots. (i) UV-vis absorption spectrum (red) and fluorescence emission spectrum (blue) of the MA-dots solution (excitation wavelength from left to right: 360, 380, 420, 440, 460, and 480 nm).

bonds were formed within the carbon skeleton, ultimately resulting in the final aromatic structure of the MA-dots and conferring their fluorescence properties. The presence of L-arginine passivation agents significantly enhanced the stability and hydrophilicity of the MA-dots.

FT-IR and XPS spectra were obtained to gain deeper insight into the chemical structure and composition of the MA-dots. Notably, several characteristic vibrational signatures attributed to guanidine groups were observed in the FT-IR spectrum of the MA-dots (Fig. 1b), including C–N–C bending vibrations at 537 cm^{-1}, C–N stretching vibrations at 1159 cm^{-1}, C=N stretching vibrations at 1052 and 1631 cm^{-1}, N–H wagging vibrations at 996 cm^{-1}, and N–H stretching vibrations at 3176, 3212, 3320, and 3409 cm^{-1}.[29,30] This confirmed the retention of guanidine groups during incomplete polymerization. The presence of C=O stretching vibrations at 1686 cm^{-1} indicated the inheritance of the carbonyl group from L-arginine.[31] The appearance of new peaks at 806, 925, 1271, 1324, 1412, and 1484 cm^{-1} provided strong evidence for the formation of the triazine rings within the MA-dots.[32–34] Furthermore, a new peak at 2036 cm^{-1} indicated the presence of triple bonds and cumulative double bonds in the MA-dot structure.[35]

According to the XPS results of the MA-dots, their composition consisted of 61.01% carbon (C), 29.24% nitrogen (N), and 9.75% oxygen (O) (Fig. 1c). The theoretical and actual compositions of the MA-dots were compared (Table S1†). The theoretical compositions of the MA-dots were estimated based on the initial feed amount of the carbon source. Given the significantly higher elemental stability of carbon compared to nitrogen and oxygen, it was assumed that no loss occurred in the carbon content of the initial carbon source during the formation of MA-dots. Thus, the carbon from the initial carbon source was fully utilized for constructing the MA-dots. Under this premise, it was observed that the actual nitrogen content decreased by 14.33% compared with the theoretical value. This finding supports the occurrence of deamidation during the formation of the MA-dots.

The XPS C 1s spectrum of the MA-dots revealed four contributions arising from C–H/C–C/C=C, C–N/C–O, C=N/O=C–NH, and –COOH species, located at 284.60 eV (1.59, 43.90%), 285.76 eV (1.49, 22.99%), 287.24 eV (1.81, 17.88%), and 288.33 eV (2.2, 15.23%), respectively (Fig. 1d),[36] with the full width at half-maximum and relative peak areas provided in parentheses. Concerning the XPS N 1s states of the MA-dots, three peaks at 398.10 eV (1.41, 24.57%), 399.16 eV (1.47, 29.52%), and 400.03 eV (1.92, 45.91%) were attributed to primary (NH_2), secondary (NH), and tertiary amine (N) groups, respectively (Fig. 1e).[36] Compared to the theoretical nitrogen composition, the primary and secondary amine groups within the MA-dots decreased by 10.43% and 25.48%, respectively, while the tertiary amine increased by 35.91% (Table S2†). This outcome further corroborates the generation of the triazine structure, which is characterized by a significant presence of tertiary amine groups. The XPS O 1s spectrum of the MA-dots displayed peaks at 531.33 eV (2.06, 75.57%) and 532.90 eV (2.18, 24.43%), consistent with the presence of C=O and C–OH functional groups (Fig. 1f),[37] indicating the retention of characteristic amino acid functional groups in the MA-dots, even after the partial loss of $-NH_2$ and –COOH functional groups during the aromatization and carbonation processes.

The MA-dots exhibited a uniform and mono-dispersed spherical nanoparticle morphology (Fig. 1g), with an average particle diameter of approximately 3.5 nm. In the XRD patterns of the MA-dots, a prominent and broad diffraction peak was observed at approximately 24° (Fig. 1h), corresponding to the (002) plane of the graphitic carbon. This peak confirmed the graphene structure of the MA-dots.[38,39] The ultrasmall size of the MA-dots enables them to easily traverse the gut mucosal barriers following oral administration.[40] Additionally, excess MA-dots with ultrasmall dimensions in the systemic circulation can be efficiently eliminated through renal clearance,[41] significantly reducing their toxicity *in vivo*. Furthermore, the resulting MA-dots displayed a robust absorption peak at 208 nm, which was attributed to the π–π^* transition of the aromatic C=C bonds (Fig. 1i).[42] This absorption can be converted into fluorescence emission. Owing to quantum confinement effects, the fluorescence emission of the MA-dots is dependent on the excitation wavelength (Fig. 1i), with emission peaks red-shifting as the excitation wavelength increases. The most pronounced fluorescence emission spectrum of the MA-dots was centered at 404 nm when excited at 340 nm. The autofluorescence of the MA-dots can likely be attributed to their triazine structure, which promotes chromophore formation, combined with their exceptionally small size, contributing to the quantum confinement effect.[43–45] The quantum yield (QY) of the MA-dots was determined to be 15.12% using quinine sulfate as a standard (Fig. S1†).

3.2. *In vitro* antitumor effect of the MA-dots

The evaluation of antitumor activity *in vitro* involved monitoring the survival status of A549 cells incubated with the MA-dots. BEAS-2B cells were used as controls to assess the cytotoxicity of MA-dots. The MA-dots exhibited noticeable antitumor activity at a minimum concentration of 50 μg mL^{-1} (Fig. 2a), resulting in the death of 17.20% of A549 cells. A549 cells treated with MA-dots (100 μg mL^{-1}) for 24 h displayed characteristic apoptotic morphology, inducing cell shrinkage (Fig. S2†). The IC_{50} of A549 cells treated with MA-dots was determined to be 93.60 μg mL^{-1} (Fig. 2c), representing over a 12-fold reduction compared to metformin-treated cells (IC_{50} = 1159.00 μg mL^{-1}). Notably, the effective concentration of metformin in the antitumor process was even lower when considering the actual feeding amount of metformin used to prepare the MA-dots. In contrast, when equal doses of L-arginine and metformin were tested within the chosen concentration range (0–200 μg mL^{-1}), virtually no antitumor activity was observed (Fig. 2a). Additionally, the highest tested concentration of the MA-dots (200 μg mL^{-1}) did not exhibit cytotoxicity against non-cancerous BEAS-2B cells (Fig. 2b), which maintained their morphology with almost no changes after treatment with MA-dots (100 μg mL^{-1}) for 24 h (Fig. S2†). Similar results were obtained in experiments involving other tumors and non-cancerous cell lines. The

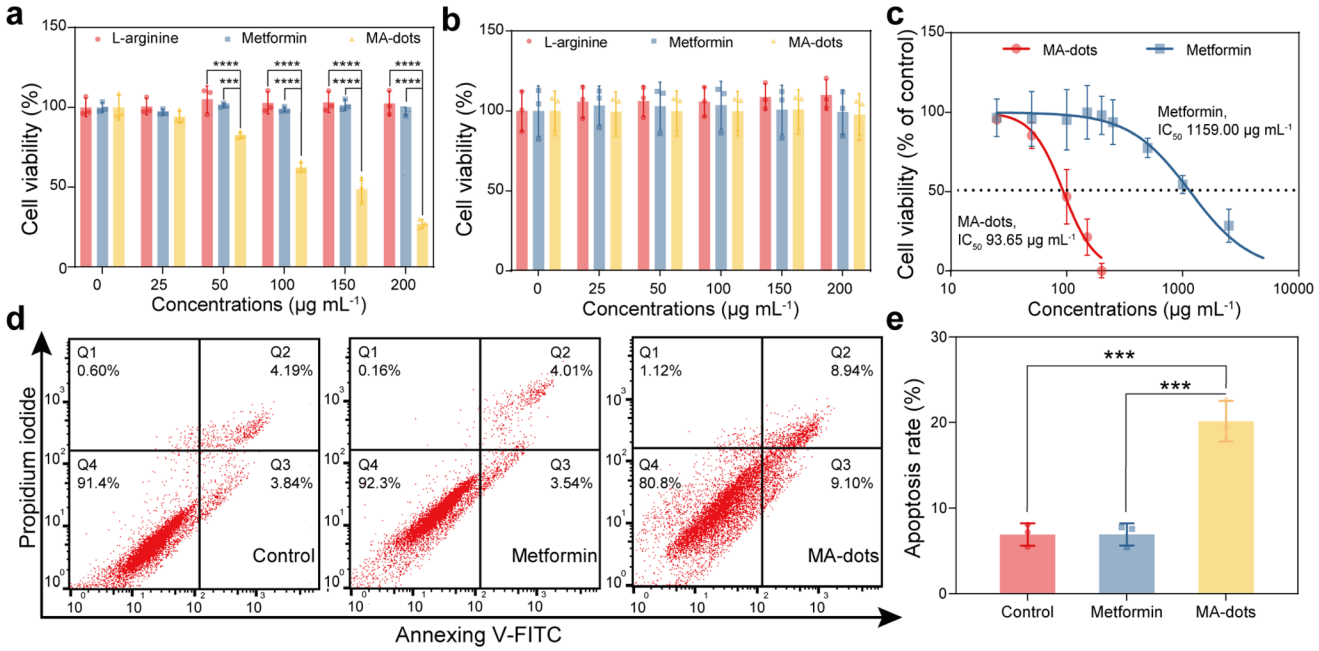

Fig. 2 *In vitro* antitumor effect of the MA-dots. The viability of the A549 (a) and the BEAS-2B (b) cells treated with various concentrations of the MA-dots, metformin, or L-arginine (0, 25, 50, 100, 150, and 200 μg mL^{-1}) for 24 h. n = 3. (c) The IC_{50} of the A549 cells was treated with various concentrations of MA-dots or metformin. n = 3. (d) Flow cytometry analysis of A549 cells treated with MA-dots or metformin (50 μg mL^{-1}) for 24 h. (e) The apoptosis rate of the A549 cells treated with the MA-dots or metformin (50 μg mL^{-1}) for 24 h. n = 3. Data display mean ± s.d. (two-way ANOVA analysis for (a) and (b), one-way ANOVA analysis for (e), ***p < 0.001 and ****p < 0.0001).

MA-dots demonstrated inhibitory effects on HepG2 (liver cancer cell lines), MCF-7 (breast cancer cell lines), and HeLa cells (cervical cancer cell lines), with minimal effects on NCTC1469 (normal liver cell lines) and HEK293 (normal human embryonic kidney 293 cell lines) cells (Fig. S3†). When comparing the IC_{50} values of free metformin and encapsulated metformin, it was evident that the effective concentration of the MA-dots in the antitumor process was lower than that in other metformin delivery nanosystems (Table S3†). These findings led to the conclusion that microwave-induced nanosizing of metformin significantly enhances its antitumor activity while maintaining low toxicity to normal cells.

Annexin V-FITC/PI double staining was used to assess the degree of apoptosis in the tumor cells (Fig. 2d and e). After 24 h of treatment with MA-dots (50 μg mL^{-1}), 20.10% of A549 cells underwent apoptosis, accounting for the reduction in cell counts. Cell proliferation and growth are intricately governed by the orderly progression of cell cycle stages, including the G0 (gap 0), G1 (gap 1), S (synthesis), G2 (gap 2), and M (mitosis) phases. Dysregulation of the cell cycle can lead to rapid cell proliferation and induce carcinogenesis,[46] making it an intriguing target for tumor treatment.[47] Cell cycle analysis of A549 cells stained with PI was conducted to determine which cell cycle stage was affected by MA-dots. The cell cycle comprises five phases: G0, G1, S, G2, and M. Flow cytometry analysis, based on the DNA content, identifies these cell cycle stages, including G0/G1, S, and G2/M phases. Following treatment with MA-dots, the cell cycle was predominantly arrested at the S and G2/M phases, while the cell population in the G0/G1 phase decreased by 18.25% compared to that in the metformin-treated group (Fig. S4†). This observation indicated that MA-dots suppressed DNA replication and mitosis. Notably, the cell cycle-dependent antitumor mechanism of the MA-dots differed from that of high concentrations of metformin. Tumor cells exposed to high concentrations of metformin are mainly arrested at the G0/G1 stage,[48] and metformin primarily interferes with the synthesis of RNA and proteins to form spindles. Additionally, the progression of cells through the S and G2/M phases is regulated by cyclin A2 and cyclin B1.[49,50] Consistent with the flow cytometry results, western blot demonstrated that cyclin A2 and cyclin B1 levels were downregulated after 24 h of exposure to the MA-dots (Fig. S5†).

3.3. Tumor targeting effect of the MA-dots

The heightened antitumor activity of the MA-dots is attributed to their superior cell uptake efficiency compared to that of metformin alone. To achieve this, L-arginine was introduced to confer tumor-specific targeting capabilities to MA-dots. These L-arginine-decorated MA-dots act as large neutral amino acid analogs capable of binding to the highly expressed LAT1 proteins found in the membranes of various human tumor cells. LAT1 proteins play a crucial role in supplying amino acids and essential nutrients to rapidly proliferating tumor cells.[51] The characteristic of being large neutral amino acid analogs makes MA-dots more readily internalized by tumor cells than by normal cells. The tumor-specific targeting ability of the MA-dots was assessed by observing their interaction with cells by fluorescence microscopic imaging and flow cytometry analysis.

Fluorescence imaging revealed that the MA-dots selectively penetrated the A549 cells, predominantly residing in the cytoplasm (Fig. 3a). In contrast, their presence in the BEAS-2B cells was barely detectable. This strong evidence confirmed the high tumor-selective uptake capacity of the MA-dots. Quantitative analysis using flow cytometry demonstrated that the cellular uptake rate of MA-dots in A549 cells was 84.30%, which was approximately 18-fold higher than that in BEAS-2B cells (4.70%) (Fig. 3b and Fig. S6†). This substantial difference in tumor-specific cell uptake efficiency enhances the biodistribution of the MA-dots, maximizes their antitumor effectiveness, and minimizes their potential toxicity to healthy cells. Additionally, the autofluorescence exhibited by MA-dots makes them suitable as fluorescent nanoprobes for tumor imaging or labeling.

The inclusion of L-arginine in the modification of metformin serves the dual purpose of stabilizing the nanostructure and imparting MA-dots with the characteristics of the large neutral amino acid analogs. Structural characterization confirmed that the MA-dots retained the characteristic functional groups of the amino acids. To confirm their status as large neutral amino acid analogs of the MA-dots, various large neutral amino acid distracters were co-incubated with A549 cells and MA-dots. These distracters included Phe, Leu, and Gly, and BCH. Both Leu and Phe exhibited a higher binding affinity for LAT1 proteins than Gly.[52] LAT1 can also be targeted for cancer therapy, and LAT1 inhibitors, such as BCH, can inhibit amino acid transport in tumor cells, thereby suppressing their proliferation.[53]

The experimental results demonstrated that the uptake of MA-dots by tumor cells was inhibited by over 50% in the presence of Leu, Phe, and BCH, while Gly had virtually no effect on MA-dot uptake by tumor cells (Fig. 3c and Fig. S7†). The co-presence of MA-dots or BCH did not synergistically strengthen the antitumor effect (Fig. 3d). Conversely, the antitumor effect of MA-dots at higher concentrations (150 and 200 μg mL^{-1})

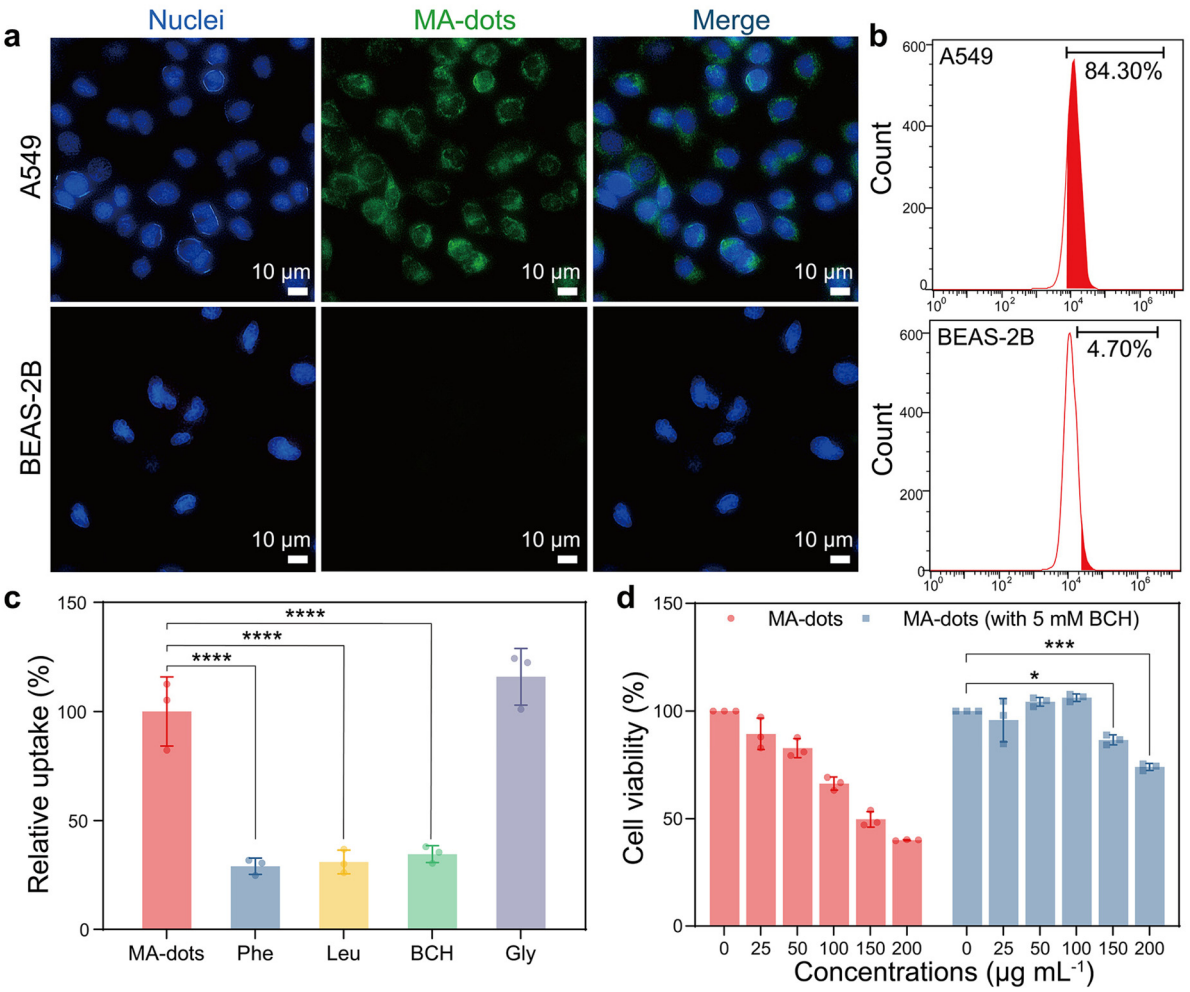

Fig. 3 Tumor targeting effect of the MA-dots. (a) Fluorescence images of the A549 and the BEAS-2B cells treated with MA-dots (100 μg mL^{-1}) for 6 h (blue fluorescence (λ_{ex} = 365 nm): nuclei, green fluorescence (λ_{ex} = 488 nm): the MA-dots). Scale bar = 10 μm. (b) Cellular uptake of the MA-dots (100 μg mL^{-1}) in the A549 and the BEAS-2B cells at 6 h using flow cytometry analysis. (c) The cellular uptake rate of the MA-dots in the A549 cells in the presence of Leu, Phe, Gly, or BCH (5 mM). n = 3. (d) Cell viability of the A549 cells treated with MA-dots (100 μg mL^{-1}) in the presence of BCH (5 mM) by MTT assay. n = 3. Data display mean ± s.d. (one-way ANOVA analysis, *p < 0.05, ***p < 0.001, and ****p < 0.0001).

decreased by more than 30% in the presence of BCH. This result reinforces the notion that BCH inhibits the expression of LAT1, thereby blocking the uptake of MA-dots by tumor cells and affecting their antitumor activity.

The internalization process of the MA-dots was further investigated, focusing on two major pathways used by eukaryotic cells to internalize extracellular substances through membrane deformation: clathrin- and caveolin-mediated endocytosis.[54] Chlorpromazine, a clathrin inhibitor, and genistein, a caveolin inhibitor, were introduced in the context of BCH, serving as controls. Both chlorpromazine and BCH inhibited the internalization of the MA-dots by more than 50% (Fig. S8†). In contrast, genistein did not significantly affect the uptake of the MA-dots. This result confirmed the internalization of the MA-dots through the mechanism of clathrin-mediated endocytosis.

3.4. Mitochondrial damage effect of the MA-dots

This prevailing perspective suggests that metformin exerts its antitumor effects by interfering with the metabolism of tumor cells.[55,56] The properties of metformin passed down to the MA-dots may have conferred a high affinity for mitochondria,[57] resulting in excellent mitochondria-targeting capabilities. To further analyze the colocalization of MA-dots within mitochondria after 8 h of incubation in A549 cells, we scrutinized the fluorescence images in Fig. 4a. These images reveal that MA-dots effectively enter the mitochondria, exhibiting a Pearson's

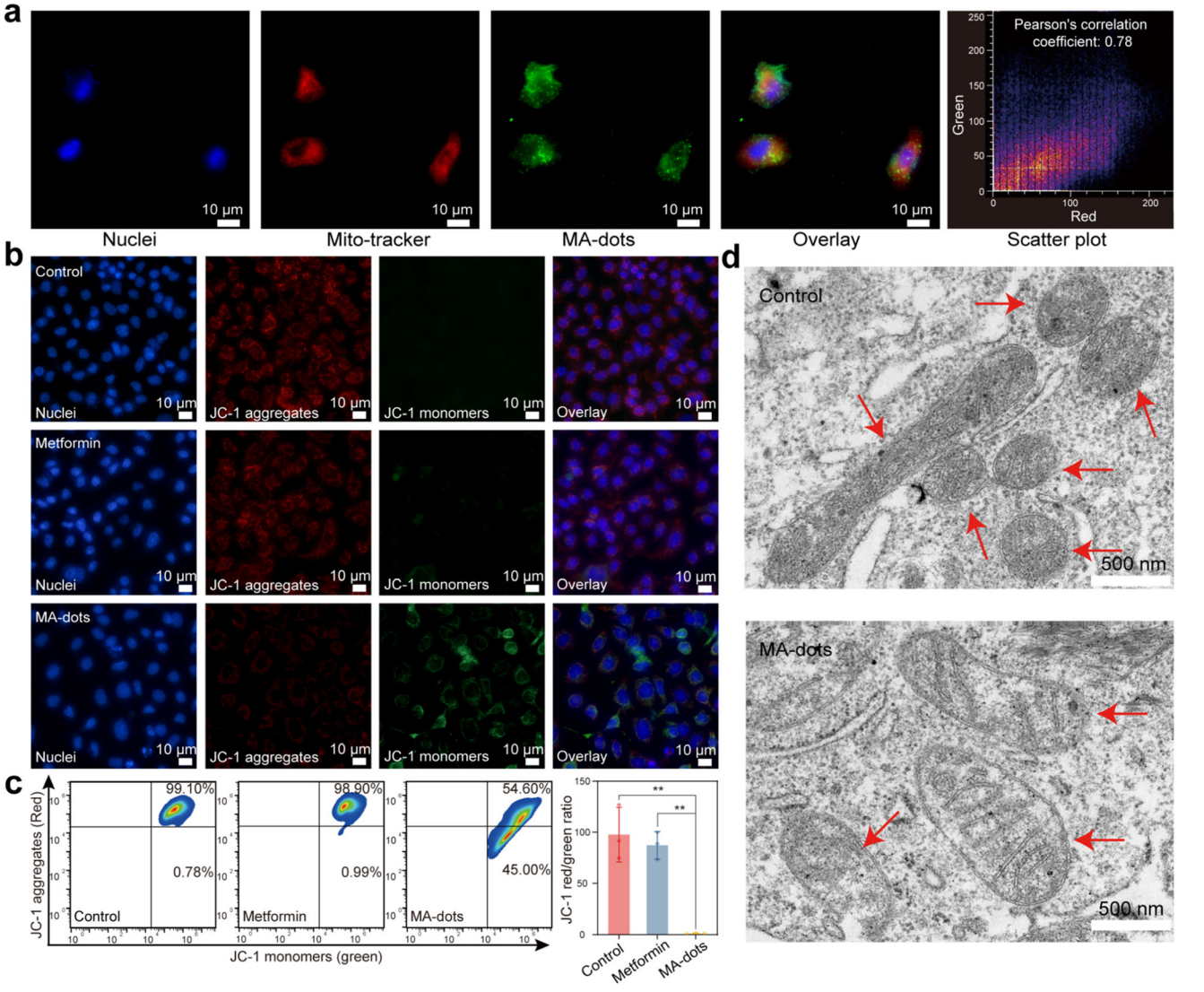

Fig. 4 Mitochondrial damage effect of the MA-dots. (a) Fluorescence images (scale bar = 10 μm) of A549 cells incubated with MA-dots (100 μg mL^{-1}) and Mito-Tracker Green (λ_{ex} = 644 nm). (b) Fluorescence imaging (scale bar = 10 μm) of the mitochondrial membrane potential (MMP) of the A549 cells treated with the MA-dots or metformin (100 μg mL^{-1}) using JC-1 staining as an MMP-specific marker (λ_{ex} = 514, 585 nm). (c) Flow cytometry analysis of the mitochondrial membrane potential (MMP) of the A549 cells treated with the MA-dots or metformin (100 μg mL^{-1}) using JC-1 staining as an MMP-specific marker. n = 3. (d) TEM images (scale bar = 500 nm) of the mitochondria of the A549 cells treated with or without the MA-dots (100 μg mL^{-1}). Arrows point to mitochondria. Data display mean ± s.d. (one-way ANOVA analysis, $^{**}p < 0.01$).

correlation coefficient of 0.78, signifying their exceptional mitochondrial targeting ability.

Tumor cells, characterized by their rapid and uncontrolled growth, undergo abnormally accelerated energy metabolism compared with normal cells.[58,59] This metabolic trait renders tumor cells susceptible to interference in energy metabolism. Some antitumor drugs have been designed based on this metabolism-perturbing mechanism, in which mitochondrial function plays a pivotal role in cellular energy metabolism. Therefore, certain drugs, such as metformin, directly interfere with energy metabolism and damage mitochondrial structure and function.[60] Herein, we assessed the impact of MA-dots on the mitochondria of tumor cells through MMP, mitochondrial morphology, ROS levels, and signaling pathways.

A decline in MMP serves as an indicator of mitochondrial damage and dysfunction,[61] and is a parameter assessed by JC-1 staining.[62] Both fluorescence microscopy and flow cytometry analyses were employed to observe the aggregation status of JC-1 molecules. JC-1 monomers (green fluorescence, low potential) were dispersed in the cytoplasm in the presence of MA-dots, and JC-1 aggregates (red fluorescence, high potential) exhibited a significant reduction of approximately 50% (Fig. 4b and c). This outcome underscores a decline in MMP and the disruption of MMP by MA-dots. In contrast, metformin at the same concentration had almost minimal effect on the mitochondrial membrane permeability of tumor cells.

Furthermore, the mitochondrial morphology exhibited significant alterations in the presence of MA-dots (Fig. 4d). Under the influence of these nanoparticles, mitochondria swelled with a lower matrix density. The mitochondrial cristae, which are essential for mitochondrial structure and function, appeared irregular and diminished compared to those of the control group. Mitochondrial damage typically coincides with increased ROS levels.[63] Elevated ROS levels were observed in A549 cells treated with MA-dots, providing additional evidence for mitochondrial damage (Fig. S9 and S10†). High levels of ROS can further impede tumor growth,[64,65] augmenting the antitumor effect of the MA-dots.

AMPK and mTOR play pivotal roles in cellular energy metabolism.[66,67] Some studies have proposed that the antitumor activity of metformin, based on the mitochondrial damage mechanism, may be mediated by activation of the AMPK pathway and inhibition of the mTOR pathway.[68] To ascertain the signaling pathway involved in the antitumor process of MA-dots, we investigated the expression of AMPK and mTOR in A549 cells treated with MA-dots *via* western blot analysis.

The results revealed that the MA-dots increased the phosphorylation/activation of AMPK 0.28-fold, while reducing the phosphorylation/activation of mTOR 1.11-fold in tumor cells compared to that in the metformin group (Fig. S11†). This phenomenon also occurs in the presence of high concentrations of metformin.[67,68] However, low concentrations of metformin, equivalent to those of MA-dots, had minimal effects on these two pathways. Activation of the AMPK pathway can influence various pathophysiological activities related to tumor growth and metabolism, including the inhibition of cellular proliferation and induction of a high level of autophagy.[69,70] mTOR, a downstream target of AMPK, is involved in intracellular nutrient-sensing by controlling protein synthesis during cell growth and metabolism.[71] Overactivation of mTOR is associated with tumor progression and resistance to chemotherapy resistance.[72] Therefore, regulating the AMPK/mTOR pathway is a promising therapeutic target for antitumor treatment, solidifying the evidence for the antitumor capabilities of MA-dots.

3.5. *In vivo* antitumor effect and safety of the MA-dots

Therapeutic evaluation of MA-dots was further conducted in A549 tumor-bearing mice. Following intragastric administration (100 mg kg^{-1}), the MA-dots exhibited a tumor-suppressive effect *in vivo* (Fig. 5a–e) without any toxicity, as evidenced by measurements of body weight (Fig. 5f). In comparison, the tumor volume in the control and metformin group rapidly increased 3.21- and 1.34-fold, respectively.

These results are consistent with those obtained in the *in vitro* cell experiments. Additionally, cell proliferation and apoptosis in the tumor tissues were analyzed. The tumor tissues from each group on day 14 were harvested after intragastric administration and subjected to H&E staining and immunohistochemistry methods, including the Ki67 assay and TUNEL assay (Fig. 5g). The experimental results showed that tumors from mice treated with MA-dots displayed the highest apoptosis rate and lowest proliferation level compared to the other control groups.

The expression of AMPK and mTOR in tumor tissues was also assessed by western blot analysis. Mice administered MA-dots exhibited increased phosphorylation/activation of AMPK and significantly decreased phosphorylation/activation of mTOR compared to metformin-administered mice (Fig. 5h and k). This result was consistent with the protein expression trends observed in the *in vitro* cell experiments (Fig. S11†). Regarding p-AMPKα expression levels, there was a significant difference in the tumor tissues of MA-dot-treated mice (1.61-fold increase) compared with those of the control group. However, the difference was not significant when compared with the metformin-treated group (0.53-fold improvement). Conversely, alterations were more pronounced in p-mTOR expression in the tumor tissues of MA-dot-treated mice. Relative to the control and the metformin-treated group, the MA-dot group exhibited a notably lower p-mTOR expression, by 1.37-fold and 0.74-fold, respectively. Therefore, concerning the combined protein expression levels observed in both *in vivo* and *in vitro* experiments, it is likely that MA-dots primarily exert their effects through the activation/phosphorylation of p-mTOR.

The tumor-specific targeting ability of the MA-dots *in vivo* was also confirmed during administration. Mice were sacrificed at 2, 4, 6, 16, and 24 h after oral administration of the MA-dots. The major organs and tumors were collected and observed using an *in vivo* imaging system (IVIS). MA-dots were distributed in the stomach and small intestine after 2 h

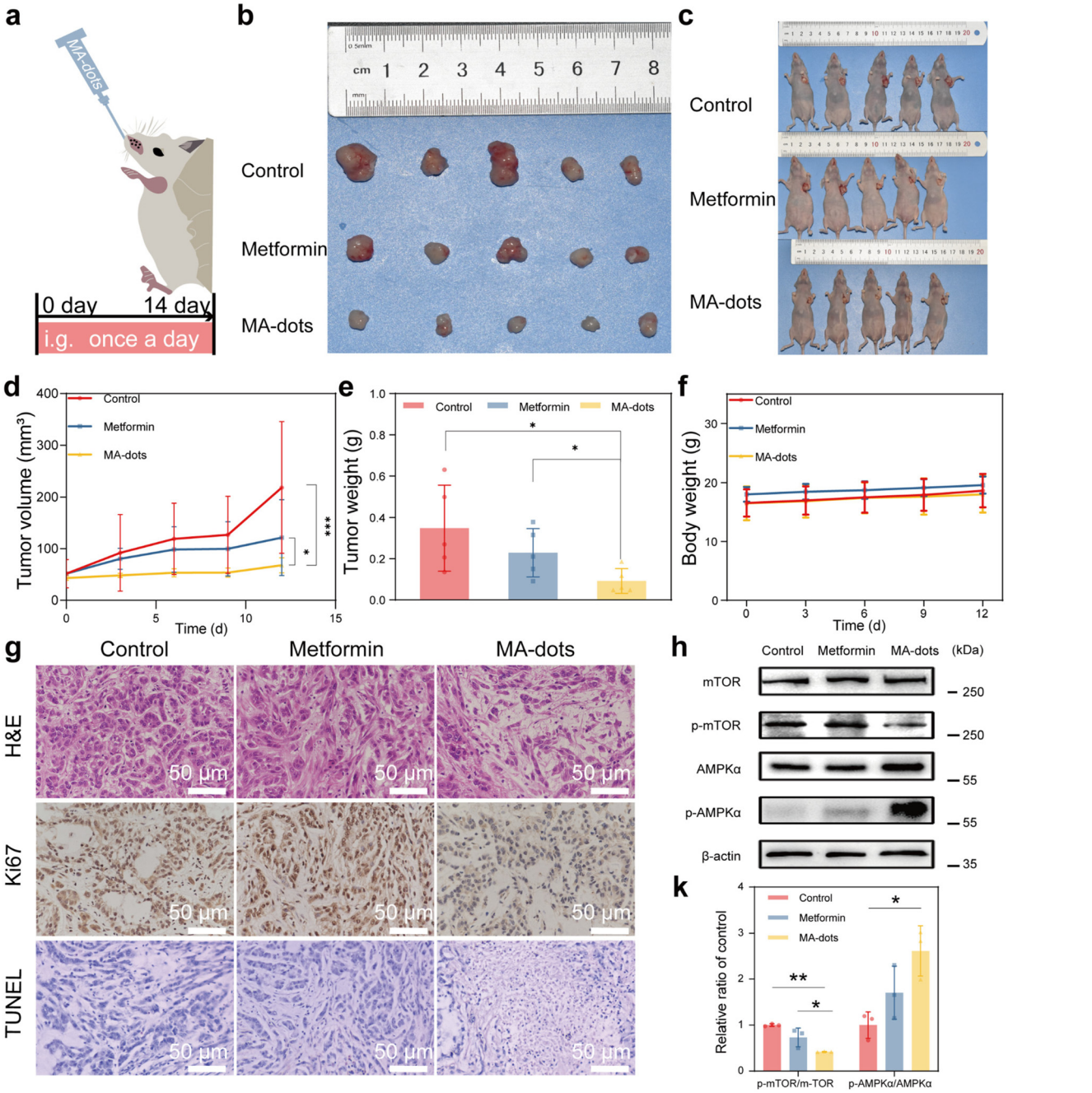

Fig. 5 *In vivo* antitumor effect of the MA-dots. (a) Mice received daily gavage of the drug for 14 days at 100 mg kg^{-1}. (b) Tumor images of the mice on day 14 treated with metformin or MA-dots. (c) Images of the mice treated with metformin or MA-dots for 14 days. (d) Tumor volume growth curves of the mice treated with metformin or the MA-dots. n = 5. (e) Final tumor weight. (f) Body weight of A549 tumor-bearing mice. (g) Tumor tissues (stained by H&E, Ki67, or TUNEL) of the mice on day 14 treated with metformin or the MA-dots. Scale bars = 50 μm. (h) and (k) Western blot analysis of AMPK, p-AMPK, mTOR, and p-mTOR expression in the tumor tissues of the mice on day 14 treated with metformin or the MA-dots. n = 3. Data display mean ± s.d., (one-way ANOVA analysis for (d), (e), and (k), *p < 0.05, **p < 0.01, and ***p < 0.001).

(Fig. S12a†). Some of them penetrate the digestive system and enter the bloodstream and liver (Fig. S12b†), which are the primary sites for drug metabolism. The MA-dots began to accumulate in the tumors after 4 h (Fig. S12b†), demonstrating the *in vivo* tumor-specific targeting ability of the MA-dots. The highest level of MA-dots in the tumors was reached at 6 h (Fig. S12b†), with some MA-dots appearing in the kidneys for renal excretion. At 16 h, the presence of MA-dots in the small intestine significantly declined, while their retention in the stomach remained relatively stable compared to that at 6 h. This suggested that, similar to most orally administered drugs, the small intestine served as the main absorption site for most

MA-dots. Even at 24 h, MA-dots were still observed in the digestive system, indicating a prolonged gastric retention time and gastric emptying time, which contribute to high bioavailability.

Furthermore, the MA-dots exhibited a high retention rate and long duration (within 4–24 h) in the tumor area, allowing them to fully exert their therapeutic effect. In summary, the MA-dots demonstrated *in vivo* tumor-specific targeting treatment effects and non-specific distribution in the stomach, small intestine, liver, and kidneys, which are related to absorption, metabolism, and excretion, respectively. No MA-dots were detected in the heart, spleen, or lungs, confirming their relative safety in these organs.

The *in vivo* safety of the MA-dots was further evaluated using healthy female BALB/c mice through daily quantitative oral gavage for 7 days (6 weeks old, n = 5 per group). Data on body weight, blood chemistry, and histopathological profiles were also collected. Administration of the MA-dots did not induce any observable toxicity in the mice (Fig. S13a†). Even the mice treated with the highest dose (400 mg kg^{-1} day^{-1}) of MA-dots developed normally and were indistinguishable from the control group. Furthermore, there was no evidence of hepatic or renal toxicity in these mice, as indicated by the normal levels of liver and renal function markers, including alanine aminotransferase, alkaline phosphatase, aspartate aminotransferase, creatinine, and blood urea nitrogen (Fig. S13b–f†). Organs, including the heart, liver, spleen, lungs, and kidneys, were harvested from the treated mice and subjected to H&E staining. These organs showed minimal discrepancies compared with those of the control group (Fig. S14†). The accumulation of MA-dots in the liver and kidneys did not result in any specific or obvious organ damage. These results collectively demonstrate that oral administration of the MA-dots had negligible local or systemic toxicity. Both the *in vitro* and *in vivo* experimental findings support the conclusion that MA-dots exhibit an acceptable intrinsic safety profile for potential human use in tumor therapy.

4. Conclusions

In summary, we developed a novel nanomedicine (MA-dots) using metformin and L-arginine through a simple microwave-based strategy. Extensive *in vitro* and *in vivo* evidence has confirmed that MA-dots possess excellent biocompatibility and demonstrate potent antitumor activity. The IC_{50} of the A549 cell lines treated with MA-dots was 93.60 μg mL^{-1}, which was over 12-fold lower than that of metformin (IC_{50} = 1159.00 μg mL^{-1}). These MA-dots exhibit the ability to target tumor cells *in vitro* and *in vivo* by binding to the highly expressed LAT1 proteins in malignant cell membranes. Their autofluorescence also allows tumor tissue and cell labeling and imaging both *in vitro* and *in vivo*. Upon entering tumor cells, they accumulate in the mitochondria, leading to mitochondrial damage and disruption of energy metabolism by disrupting the AMPK/mTOR pathway. This straightforward, safe, and effective nanomedicine offers new possibilities for the design and preparation of therapeutic agents based on existing molecular drugs. It has the potential to significantly shorten the research and development timeline for drugs in high-demand areas, thereby advancing the concept of "new uses of old drugs". Current research also holds promise for advancing the use of metformin in tumor treatment.

Ethical statement

All animal procedures were performed in accordance with the Guidelines for Care and Use of Laboratory Animals of China Medical University and experiments were approved by the Animal Ethics Committee of China Medical University.

Author contributions

Manling Chen: conceptualization, investigation, writing – original draft, writing – review and editing, and formal analysis. Yang Li: resources, investigation, and funding acquisition. Yangcheng Liu: investigation. Baohua Jia: writing – review and editing. Xue Liu and Tianyi Ma: resources, conceptualization, funding acquisition, and writing – review and editing. All authors discussed and commented on the manuscript.

Conflicts of interest

There are no conflicts to declare.

Acknowledgements

TYM acknowledges the National Natural Science Foundation of China (No. 52071171, 52202248), the Liaoning BaiQianWan Talents Program (LNBQW2018B0048), the Shenyang Science and Technology Project (21-108-9-04), the Key Research Project of Department of Education of Liaoning Province (LJKZZ20220015), the Australian Research Council (ARC) through Future Fellowship (FT210100298, FT210100806), the Discovery Project (DP220100603), the Linkage Project (LP210100467, LP210200504, LP210200345, LP220100088), and Industrial Transformation Training Centre (IC180100005) schemes, and the Australian Government through the Cooperative Research Centres Projects (CRCPXIII000077). XL acknowledges the National Natural Science Foundation of China (51873085), the Natural Science Foundation of Liaoning Province-Outstanding Youth Foundation (2022-YQ-14), the Liaoning Revitalization Talents Program (XLYC2007056), and the China Scholarship Council (CSC Scholarship No. 202006800009). YL acknowledges the Project of Science and Technology Department of Liaoning Province (2022-MS-197).

References

1 N. Wu, C. Gu, H. Gu, H. Hu, Y. Han and Q. Li, *Neoplasma*, 2011, **58**, 482–490.
2 J. L. Wang, Y. W. Lan, Y. T. Tsai, Y. C. Chen, T. Staniczek, Y. A. Tsou, C. C. Yen and C. M. Chen, *Front. Cell Dev. Biol.*, 2021, **9**, 688062.
3 F. M. Zi, J. S. He, Y. Li, C. Wu, L. Yang, Y. Yang, L. J. Wang, D. H. He, Y. Zhao, W. J. Wu, G. F. Zheng, X. Y. Han, H. Huang, Q. Yi and Z. Cai, *Cancer Lett.*, 2015, **356**, 443–453.
4 J. M. M. Evans, L. A. Donnelly, A. M. Emslie-Smith, D. R. Alessi and A. D. Morris, *Br. Med. J.*, 2005, **330**, 1304–1305.
5 S. L. Bowker, S. R. Majumdar, P. Veugelers and J. A. Johnson, *Diabetes Care*, 2006, **29**, 254–258.
6 S. Yendamuri, J. Barbi, S. Pabla, C. Petrucci, A. Punnanitinont, M. Nesline, S. T. Glenn, P. Depietro, A. Papanicalou-Sengos, C. Morrison, G. K. Dy and P. L. Elkin, *J. Thorac. Oncol.*, 2019, **14**, 2181–2187.
7 M. P. Quaile, D. H. Melich, H. L. Jordan, J. B. Nold, J. P. Chism, J. W. Polli, G. A. Smith and M. C. Rhodes, *Toxicol. Appl. Pharmacol.*, 2010, **243**, 340–347.
8 G. G. Graham, J. Punt, M. Arora, R. O. Day, M. P. Doogue, J. K. Duong, T. J. Furlong, J. R. Greenfield, L. C. Greenup, C. M. Kirkpatrick, J. E. Ray, P. Timmins and K. M. Williams, *Clin. Pharmacokinet.*, 2011, **50**, 81–98.
9 C. R. Chong and B. A. Chabner, *Oncologist*, 2009, **14**, 1178–1181.
10 S. Kordes, M. N. Pollak, A. H. Zwinderman, R. A. Mathôt, M. J. Weterman, A. Beeker, C. J. Punt, D. J. Richel and J. W. Wilmink, *Lancet Oncol.*, 2015, **16**, 839–847.
11 S. R. Salpeter, E. Greyber, G. A. Pasternak and E. E. Salpeter, *Cochrane Database Syst. Rev.*, 2003, **2010**, 2594–2602.
12 J. Liu, R. Li and B. Yang, *ACS Cent. Sci.*, 2020, **6**, 2179–2195.
13 C. Xia, S. Zhu, T. Feng, M. Yang and B. Yang, *Adv. Sci.*, 2019, **6**, 1901316.
14 J. Zhang, M. Yang, X. Tang, S. Li, J. Zhang, L. Lu, Q. Wang and B. Yang, *Appl. Mater. Today*, 2022, **28**, 101544.
15 J. Liu, Y. Geng, D. Li, H. Yao, Z. Huo, Y. Li, K. Zhang, S. Zhu, H. Wei, W. Xu, J. Jiang and B. Yang, *Adv. Mater.*, 2020, **32**, 1906641.
16 Y. Liu, J. Liu, J. Zhang, X. Li, F. Lin, N. Zhou, B. Yang and L. Lu, *ACS Omega*, 2018, **3**, 7888–7896.
17 J. Liu, S. Lu, Q. Tang, K. Zhang, W. Yu, H. Sun and B. Yang, *Nanoscale*, 2017, **9**, 7135–7142.
18 G. M. Han, J. Zhao, R. L. Zhang, X. H. Tian, Z. J. Liu, A. D. Wang, R. Y. Liu, B. H. Liu, M. Y. Han, X. H. Gao and Z. P. Zhang, *Angew. Chem., Int. Ed.*, 2019, **58**, 7087–7091.
19 S. H. Li, W. Su, H. Wu, T. Yuan, C. Yuan, J. Liu, G. Deng, X. C. Gao, Z. M. Chen, Y. M. Bao, F. L. Yuan, S. X. Zhou, H. W. Tan, Y. C. Li, X. H. Li, L. Z. Fan, J. Zhu, A. T. Chen, F. Y. Liu, Y. Zhou, M. Li, X. C. Zhai and J. B. Zhou, *Nat. Biomed. Eng.*, 2020, **4**, 704–716.
20 G. M. L. Consoli, M. L. Giuffrida, C. Satriano, T. Musumeci, G. Forte and S. Petralia, *Chem. Commun.*, 2022, **58**, 3126–3129.
21 Y. Liu, J. Liu, J. Zhang, X. Li, F. Lin, N. Zhou, B. Yang and L. Lu, *Biomater. Sci.*, 2019, **7**, 1574–1583.
22 J. Liu, D. Li, K. Zhang, M. Yang, H. Sun and B. Yang, *Small*, 2018, **14**, 1703919.
23 F. Zhang, M. Zhang, X. Zheng, S. Y. Tao, Z. Q. Zhang, M. D. Sun, Y. B. Song, J. Zhang, D. Shao, K. He, J. Li, B. Yang and L. Chen, *RSC Adv.*, 2018, **8**, 1168–1173.
24 X. W. Xu, K. Zhang, L. Zhao, C. Li, W. H. Bu, Y. Q. Shen, Z. Y. Gu, B. Chang, C. Y. Zheng, C. T. Lin, H. C. Sun and B. Yang, *ACS Appl. Mater. Interfaces*, 2016, **8**, 32706–32716.
25 L. N. Wu, Y. J. Yang, L. X. Huang, Y. Zhong, Y. Chen, Y. R. Gao, L. Q. Lin, Y. Lei and A. L. Liu, *Carbon*, 2022, **186**, 452–464.
26 C. J. Lin, L. Chang, H. W. Chu, H. J. Lin, P. C. Chang, R. Y. L. Wang, B. Unnikrishnan, J. Y. Mao, S. Y. Chen and C. C. Huang, *Small*, 2019, **15**, 1902641.
27 Y. Han, F. Zhang, J. Zhang, D. Shao, Y. N. Wang, S. Li, S. Lv, G. F. Chi, M. Zhang, L. Chen and J. G. Liu, *Colloids Surf., B*, 2019, **179**, 1–8.
28 J. F. Wan, S. Q. Xu, J. Li, M. L. Yu, K. Zhang, G. Wei and Z. Q. Su, *Nanoscale*, 2022, **14**, 11359–11368.
29 K. Haruna, T. A. Saleh and M. A. Quraishi, *J. Mol. Liq.*, 2020, **315**, 113716.
30 R. M. Toudeshki, S. Dadfarnia and A. M. Haji Shabani, *Anal. Chim. Acta*, 2019, **1089**, 78–89.
31 K. Wang, Z. P. Qi, S. Pan, S. Zheng, H. S. Wang, Y. X. Chang, H. R. Li, P. Xue, X. Y. Yang and C. Fu, *RSC Adv.*, 2020, **10**, 20886–20899.
32 C. Gao, H. B. Gu, A. Du, H. Zhou, D. Pan, N. Naik and Z. H. Guo, *Polymer*, 2021, **219**, 123533.
33 B. Lin, C. Zheng, X. F. Li, Q. Y. Zhu, F. Xie and G. C. Liu, *J. Therm. Anal. Calorim.*, 2021, **147**, 1031–1040.
34 J. Wang, Y. Guo, S. P. Zhao, Z. H. Zhu, Y. Huang, T. H. Tian, Y. C. Zhou and L. H. Bi, *React. Funct. Polym.*, 2022, **178**, 105335.
35 H. X. Xu, P. H. Wang, K. J. Ning, J. S. Deng, Q. M. Zhuo and G. W. Liu, *ACS Omega*, 2019, **4**, 20503–20508.
36 Y. Cao, Y. Zhou, Y. H. Lin and J. J. Zhu, *Anal. Chem.*, 2021, **93**, 1818–1825.
37 Y. H. Chen, J. S. Lin, R. Z. Zhang, S. J. He, Z. F. Ding and L. Ding, *Analyst*, 2021, **146**, 5287–5293.
38 F. Wu, Y. S. Ye, J. Q. Huang, T. Zhao, J. Qian, Y. Y. Zhao, L. Li, L. Wei, R. Luo, Y. X. Huang, Y. Xing and R. J. Chen, *ACS Nano*, 2017, **11**, 4694–4702.
39 L. F. Lei, F. J. Pan, A. Lindbråthen, X. P. Zhang, M. Hillestad, Y. Nie, L. Bai, X. Z. He and M. D. Guiver, *Nat. Commun.*, 2021, **12**, 268.
40 M. J. Mitchell, M. M. Billingsley, R. M. Haley, M. E. Wechsler, N. A. Peppas and R. Langer, *Nat. Rev. Drug Discovery*, 2021, **20**, 101–124.
41 M. A. Dobrovolskaia, M. Shurin and A. A. Shvedova, *Toxicol. Appl. Pharmacol.*, 2016, **299**, 78–89.
42 J. Wang, M. Zhang, X. Xu, J. Feng, Y. Wang, M. Zhang, W. Han, Y. Chen and G. Tian, *Chem. Res. Chin. Univ.*, 2018, **34**, 8–12.

43 X. C. He, Y. X. Gu, S. C. Ai, M. M. Xie, Q. Lu, Y. Q. Wang and J. Q. Wang, *Appl. Surf. Sci.*, 2018, **462**, 303–309.
44 F. Munir, M. T. Waseem, Z. A. Khan, S. Majeed, U. Farooq and S. A. Shahzad, *J. Photochem. Photobiol., A*, 2022, **429**, 113921.
45 S. Shanmugaraju, D. Umadevi, L. M. Gonzalez-Barcia, J. M. Delente, K. Byrne, W. Schmitt, G. W. Watson and T. Gunnlaugsson, *Chem. Commun.*, 2019, **55**, 12140–12143.
46 C. J. Sherr, *Science*, 1996, **274**, 1672–1677.
47 G. I. Evan and K. H. Vousden, *Nature*, 2001, **411**, 342–348.
48 J. Wang, Q. Gao, D. Wang, Z. Wang and C. Hu, *Oncol. Lett.*, 2015, **10**, 1343–1349.
49 X. Xu, Y. Zhang, D. Qu, T. Jiang and S. Li, *J. Exp. Clin. Cancer Res.*, 2011, **30**, 33.
50 Y. W. Qiang, F. Ma, Z. R. Wang, Z. C. Nie, L. F. Xu, P. S. Ding and X. L. Ma, *Biochem. Biophys. Res. Commun.*, 2020, **521**, 846–852.
51 S. K. Natarajan and S. Venneti, *Cancers*, 2019, **11**, 1628.
52 H. Uchino, Y. Kanai, D. K. Kim, M. F. Wempe, A. Chairoungdua, E. Morimoto, M. W. Anders and H. Endou, *Mol. Pharmacol.*, 2002, **61**, 729–737.
53 Y. Ohshima, K. Kaira, A. Yamaguchi, N. Oriuchi, H. Tominaga, S. Nagamori, Y. Kanai, T. Yokobori, T. Miyazaki, T. Asao, Y. Tsushima, H. Kuwano and N. S. Ishioka, *Cancer Sci.*, 2016, **107**, 1499–1505.
54 V. R. Devadasu, V. Bhardwaj and M. N. Kumar, *Chem. Rev.*, 2013, **113**, 1686–1735.
55 S. R. Lord, W. C. Cheng, D. Liu, E. Gaude, S. Haider, T. Metcalf, N. Patel, E. J. Teoh, F. Gleeson, K. Bradley, S. Wigfield, C. Zois, D. R. McGowan, M. L. Ah-See, A. M. Thompson, A. Sharma, L. Bidaut, M. Pollak, P. G. Roy, F. Karpe, T. James, R. English, R. F. Adams, L. Campo, L. Ayers, C. Snell, I. Roxanis, C. Frezza, J. D. Fenwick, F. M. Buffa and A. L. Harris, *Cell Metab.*, 2018, **28**, 679–688.
56 M. Elgendy, M. Ciro, A. Hosseini, J. Weiszmann, L. Mazzarella, E. Ferrari, R. Cazzoli, G. Curigliano, A. DeCensi, B. Bonanni, A. Budillon, P. G. Pelicci, V. Janssens, M. Ogris, M. Baccarini, L. Lanfrancone, W. Weckwerth, M. Foiani and S. Minucci, *Cancer Cell*, 2019, **35**, 798–815.
57 G. Rena, D. G. Hardie and E. R. Pearson, *Diabetologia*, 2017, **60**, 1577–1585.
58 L. Galluzzi, O. Kepp, M. G. Vander Heiden and G. Kroemer, *Nat. Rev. Drug Discovery*, 2013, **12**, 829–846.
59 R. A. Cairns, I. Harris, S. McCracken and T. W. Mak, *Cold Spring Harbor Symp. Quant. Biol.*, 2011, **76**, 299–311.
60 W. W. Wheaton, S. E. Weinberg, R. B. Hamanaka, S. Soberanes, L. B. Sullivan, E. Anso, A. Glasauer, E. Dufour, G. M. Mutlu, G. S. Budigner and N. S. Chandel, *eLife*, 2014, **3**, e02242.
61 A. K. Madiraju, D. M. Erion, Y. Rahimi, X. M. Zhang, D. T. Braddock, R. A. Albright, B. J. Prigaro, J. L. Wood, S. Bhanot, M. J. MacDonald, M. J. Jurczak, J. P. Camporez, H. Y. Lee, G. W. Cline, V. T. Samuel, R. G. Kibbey and G. I. Shulman, *Nature*, 2014, **510**, 542–546.
62 S. T. Smiley, M. Reers, C. Mottolahartshorn, M. Lin, A. Chen, T. W. Smith, G. D. Steele and L. B. Chen, *Proc. Natl. Acad. Sci. U. S. A.*, 1991, **88**, 3671–3675.
63 C. Y. Tang, H. L. Han, M. J. Yan, S. Y. Zhu, J. Liu, Z. W. Liu, L. Y. He, J. Q. Tan, Y. Liu, H. Liu, L. Sun, S. B. Duan, Y. M. Peng, F. Y. Liu, X. M. Yin, Z. H. Zhang and Z. Dong, *Autophagy*, 2018, **14**, 880–897.
64 X. Sun, H. B. Xu, J. Shen, S. Y. Guo, S. Shi, J. H. Dan, F. Tian, Y. F. Tian and Y. Tian, *Ultrason. Sonochem.*, 2015, **22**, 7–14.
65 M. R. Liu, A. R. Khan, J. B. Ji, G. M. Lin, X. G. Zhao and G. X. Zhai, *J. Controlled Release*, 2018, **290**, 150–164.
66 H. X. Yuan, Y. Xiong and K. L. Guan, *Mol. Cell*, 2013, **49**, 379–387.
67 J. Xu, J. Ji and X. H. Yan, *Crit. Rev. Food Sci. Nutr.*, 2012, **52**, 373–381.
68 R. Mallik and T. A. Chowdhury, *Diabetes Res. Clin. Pract.*, 2018, **143**, 409–419.
69 Y. Yang, Q. Wang, D. J. Song, R. R. Zen, L. Zhang, Y. J. Wang, H. Y. Yang, D. Zhang, J. Jia, J. Zhang and J. X. Wang, *J. Exp. Clin. Cancer Res.*, 2020, **39**, 197.
70 X. J. Zheng, W. Li, H. L. Xu, J. Y. Liu, L. W. Ren, Y. H. Yang, S. Li, J. H. Wang, T. F. Ji and G. H. Du, *Acta Pharm. Sin. B*, 2021, **11**, 3465–3480.
71 D. R. Bolster, S. J. Crozier, S. R. Kimball and L. S. Jefferson, *J. Biol. Chem.*, 2002, **277**, 23977–23980.
72 R. A. Saxton and D. M. Sabatini, *Cell*, 2017, **168**, 960–976.